Showcasing research from Dr Wenzhong Yan at the Department of Electrical and Computer Engineering, University of California, Los Angeles, USA

Self-deployable contracting-cord metamaterials with tunable mechanical properties

Harnessing contracting-cord particle jamming, this work introduces an efficient design strategy for creating reversible, self-deployable mechanical metamaterials. These metamaterials can self-deploy into preprogrammed shapes. After deployment, their stiffness and damping can be widely tuned while preserving the shapes. They can also self-retract to their original soft state for compact transport and be ready for cyclic usage.

As featured in:
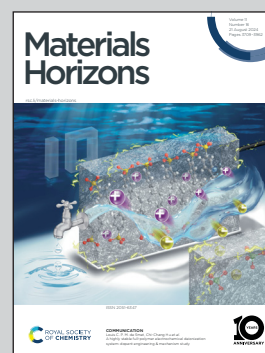
See Wenzhong Yan *et al.*,
Mater. Horiz., 2024, **11**, 3805.

ROYAL SOCIETY
OF **CHEMISTRY**

rsc.li/materials-horizons

Check for updates

Self-deployable contracting-cord metamaterials with tunable mechanical properties†

Wenzhong Yan, [ID] *[ab] Talmage Jones,[b] Christopher L. Jawetz,[bc] Ryan H. Lee,[b] Jonathan B. Hopkins [ID] [b] and Ankur Mehta[a]

Recent advances in active materials and fabrication techniques have enabled the production of cyclically self-deployable metamaterials with an expanded functionality space. However, designing metamaterials that possess continuously tunable mechanical properties after self-deployment remains a challenge, notwithstanding its importance. Inspired by push puppets, we introduce an efficient design strategy to create reversibly self-deployable metamaterials with continuously tunable post-deployment stiffness and damping. Our metamaterial comprises contracting actuators threaded through beads with matching conical concavo–convex interfaces in networked chains. The slack network conforms to arbitrary shapes, but when actuated, it self-assembles into a preprogrammed configuration with beads gathered together. Further contraction of the actuators can dynamically tune the assembly's mechanical properties through the beads' particle jamming, while maintaining the overall structure with minimal change. We show that, after deployment, such metamaterials exhibit pronounced tunability in bending-dominated configurations: they can become more than 35 times stiffer and change their damping capability by over 50%. Through systematic analysis, we find that the beads' conical angle can introduce geometric nonlinearity, which has a major effect on the self-deployability and tunability of the metamaterial. Our work provides routes towards reversibly self-deployable, lightweight, and tunable metamaterials, with potential applications in soft robotics, reconfigurable architectures, and space engineering.

New concepts

This work presents a design strategy for developing self-deployable mechanical metamaterials with continuously tunable mechanical properties after deployment. The metamaterials can self-retract back to their original soft state for compact transportation and be ready for cyclic usage. Our approach utilizes contracting-cord particle jamming (CCPJ) to achieve repeated self-deployment (and self-retraction) for compact transportation and to realize mechanical property tuning for dynamic environments. Unlike existing research, we create engineered beads with interlocking concavo–convex interfaces, threaded with contracting-cord actuators, enabling precise self-deployment into pre-programmed configurations and post-deployment tunability of mechanical properties *via* adjustable tendon-driven jamming. Post-deployment, these metamaterials exhibit significant tunability, becoming over 35 times stiffer and enhancing damping capabilities by more than 50%. This unique combination of features marks the first application of CCPJ in creating metamaterials with such properties, highlighting the substantial potential for applications in robotics, reconfigurable structures, and space engineering. Our systematic analysis of the beads' conical angles reveals their critical role in introducing geometric nonlinearity, which significantly affects the self-deployability and tunability of the metamaterials. This work provides new pathways for designing lightweight, reversible, and highly adaptable metamaterials, advancing the field of materials science with the potential for transformative applications.

Introduction

Self-deployment is widespread in nature, with examples as varied as earwig wings and peacock spider flaps.[1] Specifically, earwigs' self-deployable wings allow for both a large-area shape during flight and a compact, folded package when navigating

tight underground habitats.[2] Given its high energy efficiency, space efficiency, adaptability, and multifunctionality, this transforming strategy is widely seen in art and engineering, with applications spanning architecture, robotics, medical devices, consumer products, and aerospace technologies.[3] The length scales for these applications range from nanometers to meters.[4–10]

Recently, the concept of self-deployment has gained increasing traction in the field of metamaterials, which have attained previously untapped territories in materials property space, including negative Poisson's ratio,[11] high stiffness-to-weight ratio,[12] mechanical invisibility,[13] tunable stiffness,[14,15] *etc.*[16–19] This increasing traction is propelled by advancements in functional materials and sophisticated fabrication techniques, to achieve material-level self-deployment on demand.[20,21]

a Electrical and Computer Engineering Department, UCLA, USA.
  E-mail: wzyan24@g.ucla.edu
b Mechanical and Aerospace Engineering Department, UCLA, USA
c Woodruff School of Mechanical Engineering, Georgia Tech, USA
† Electronic supplementary information (ESI) available. See DOI: https://doi.org/10.1039/d4mh00584h
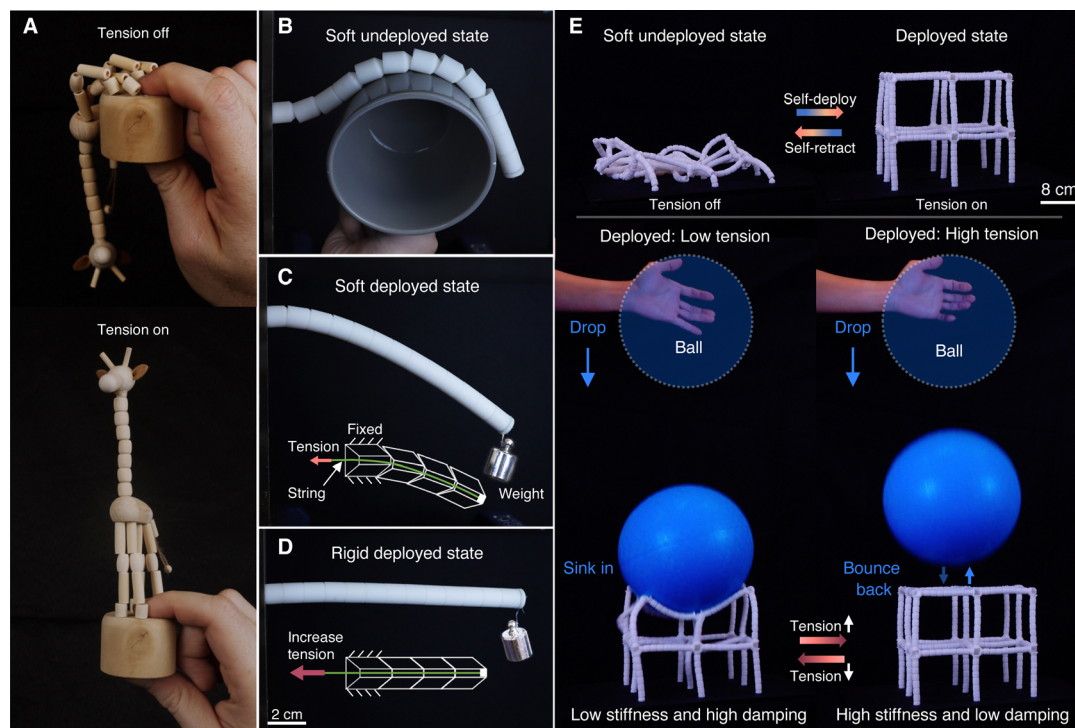
Fig. 1 The concept and prototype of the self-deployable contracting-cord mechanical metamaterials. (A) The metamaterial is inspired by push puppets. (B)–(D) The self-deployment and mechanical properties tuning process of a fundamental beam of the proposed mechanical metamaterials. (B) Image of an undeployed beam—composed of beads threaded by a contracting string-like actuator—in the soft state. (C) Self-assembly of the beads shown in b, after a contracting tension is applied through the actuator. (D) Image of the jammed beam, becoming a stiff load-bearing structure with further contraction of the actuator. (E) Self-deployment and mechanical property tuning of a 2 × 2 × 2 cubic lattice. Top: The lattice changes from a soft unassembled state to a deployed state with tension generated by the embedded actuators. Bottom: After deployment, a lattice with low string tension can capture a dropped ball by dissipating the kinetic energy through extensive damping. However, a ball dropped on the same lattice with high string tension will bounce back due to its increased stiffness. Note that the weights attached to the beam in (C) and (D) are selectively brightened in the images for visualization purposes.

Typical construction principles for self-deployable meta-materials include the use of linkages,[22,23] origami/Kirigami inspired folding-based methods,[24] and tensegrity-enabled approaches.[25,26] The transformation between configurations is often driven by phase transition,[27] strain mismatch,[24] and mechanical instability.[28,29] These driving mechanisms can be triggered by controllable physical signals, including electric current,[30,31] temperature,[32,33] magnetic fields,[34] and pneumatic pressure.[35] Once deployed, however, the metamaterials' mechanical properties are usually fixed, making each metamaterial suitable only for a specific task and limiting its applicability in unpredictable, complex environments.[15,36–39] Mechanical metamaterials with both variable stiffness and self-deployability have been demonstrated, but the two features in these materials are often coupled,[9,28,40] which limits application space. Consequently, developing mechanical metamaterials that not only can self-deploy but also retain the ability to continuously tune their mechanical properties post-deployment presents a challenge.

The realization of these self-deployable mechanical meta-materials could allow devices and machines to be stored and transported in retracted, compact states and then self-assembled to the intended configurations *in situ*. Subsequently, their mechanical properties can dynamically adjust with minimal changes in configuration, enabling them to adapt to various conditions, such as differing vibration frequency and amplitude, surface roughness, or contact stiffness. For example, a self-deployable soft robot, after assembly, can tune its limbs' stiffness to accommodate different terrains while retaining its body structure for optimal locomotion performance.[41,42] Other potential applications include impact-resistant self-assembling shelters (with enclosed shells) for air-dropping into disaster areas,[43,44] compact vibration insulators with programmable damping in dynamic environments,[45,46] and more[47,48].

To achieve such self-deployable mechanical metamaterials, a fundamentally new design paradigm is required. (i) An efficient structural construction principle—using a single actuation system for both self-deployment and mechanical properties tuning—is favorable for minimizing implementation complexity and weight. (ii) Once metamaterials are deployed, it is advantageous to maintain minimal structure variation over the tuning of mechanical properties. This is because large structure (or configuration) change might introduce undesired interference for a given application. (iii) Self-deployment should be reversible and reusable, allowing cycling and long-term operations.

Here, we present mechanical metamaterials that can reversibly self-deploy and possess post-deployment tunable stiffness

and damping based on the proposed contracting-cord particle jamming (CCPJ), inspired by push puppets (Fig. 1(A)). The core of our proposed system lies in its unique structural design, *i.e.*, CCPJ, which embodies the fundamental principles of metamaterials. The metamaterial consists of networked chains where beads are threaded along contracting actuators. A few conceptual works have examined this CCPJ mechanism, either in simple configurations[49,50] or by focusing on partial functionalities.[51] In contrast, we have uniquely engineered beads with interlocking conical concavo–convex interfaces, along with contracting-cord actuators, enabling highly precise self-deployability and a broad range of tunability in both stiffness and damping within 3D metamaterials. Detailed comparisons with other works are provided in ESI,† Table S4. We explore CCPJ-based beams experimentally and numerically by varying applied contracting tension to trigger particle jamming within engineered beads. Here, we use tension on the string to activate particle jamming, similar to other jamming (*meta*)materials, where they use other triggering actuation, such as vacuum,[52] positive pressure,[53] and electromagnetic force.[54] We also compare the results over the geometric parameter space against the underlying physics of the beads and beam. We show that a self-deployed beam has more evident tunability in its bending-dominated configuration: with an external contracting tension of 120 N, they become more than 35 times stiffer and achieve a 52% change in damping capability compared with their relaxed configuration. By varying the interfacial conical angle, the beam's self-deployability (including the alignment accuracy and success rate of assembly) and mechanical property tunability vary vastly, due to the nonlinearity arising from geometric and frictional interactions between beads.

We also characterize the mechanical tunability of CCPJ-based cubic unit cells that composed of identical unit beams, indicating the viability of using our mechanism to construct arbitrary configurations while retaining advantageous attributes. Furthermore, comparing the mechanical properties tunability of bending-dominated and stretching-dominated cells confirms the preference for bending-dominated structures in our CCPJ-based metamaterials. Specifically, our bending-dominated cubic cell exhibits a stiffness change of approximately 32 times and a 40% reduction in damping. These results show consistent performance with those observed in unit beams. In addition, we demonstrate the proposed CCPJ-based metamaterials by integrating actuators (including electrically-driven thermal artificial muscles and motor-driven cables) to enable on-demand, rapid self-deployment/self-retraction and stiffness tuning of larger scale metamaterials. Therefore, this research paves the way for a new class of materials that can self-deploy on-demand and dynamically tune their mechanical properties *in situ* to adapt to their surroundings, bringing metamaterials closer to practical applications.

Results and discussion

Design and mechanism

Fig. 1(B) shows the fundamental unit of our self-deployable contracting-cord mechanical metamaterial, *i.e.,* the particle-jamming beam. Each particle is a solid cylindrical bead with a central hole. Unlike conventional tendon-driven non-concave particle jamming,[49,55] we use beads with matching conical concavo–convex interfaces (Fig. S1, ESI†). This bead design with matching conical concavo–convex interfaces offers two primary advantages over conventional non-concave designs: (i) it facilitates alignment during self-deployment, and (ii) the surfaces provide geometrical interlocking that enhances frictional contact between adjacent beads, which results in a wide range of mechanical property changes as constraints vary[56] (see next section for more analysis). These beads are made of resin, which is manufactured with a high-resolution 3D printer based on low force Stereolithography (Form 3+, Formlabs). This printing method can produce individual beads which are fully dense and isotropic with a smooth surface; it can also fabricate beads in a rapid, programmable manner with an ample design space for arbitrary configurations (see Methods).

To apply tension and confine the beads, string-like actuators are needed, which can thread through the beads and contract/shorten upon activation. These actuators should be capable of providing sufficient contracting stroke and stress to act against resistive torque and force during the processes of both deployment and mechanical properties tuning. We chose to use two types of actuators that satisfy these requirements: motor-driven cables (MDCs) and super-coiled polymer actuators (SCPAs, which function similar to shape memory alloy.[57] See Fig. S37 for detailed characteristics). With initial slack on the actuator, the beam can freely bend, fold, and conform to curved objects (Fig. 1(B)). When activated, the actuator contracts to pull the beads together, forming a tight assembly (Fig. 1(C)). We refer to this process as self-deployment (ESI,† Movie S1). During self-deployment, the contracting actuator must supply enough tension to overcome the opposing forces and torques caused by frictional contact and gravity. Notably, the rotational symmetry of the cone-shaped interface facilitates bead alignment during this process, whereas a non-concave interface would rely solely on the actuator's tension to align the bead holes. This effect reduces inter-facial friction while greatly simplifying beam design and assembly. With further contraction of the actuator, the assembled beads can serve as load-bearing structures through particle jamming (Fig. 1(D)).[58] It is worth noting that the endpoints of the actuators are kept stationary during deformation processes (see section Quasi-Static Mechanical Tests for more details). Complex architectures can be constructed from these basic linear building units. For example, a $2 \times 2 \times 2$ cubic lattice could be created by threading beads along its edge topology (Fig. 1(E)). This lattice can self-deploy and allow variable mechanical properties after assembly, enabling distinct interactions with external loads such as a dropped ball (see section Actuating Functional Metamaterials for more details).

Tuning mechanical properties

To tune the mechanical properties of our assembled beam, we seek to trigger jamming between the beads by applying variable tension at the boundary (Fig. 1(B)). One end of the nylon string
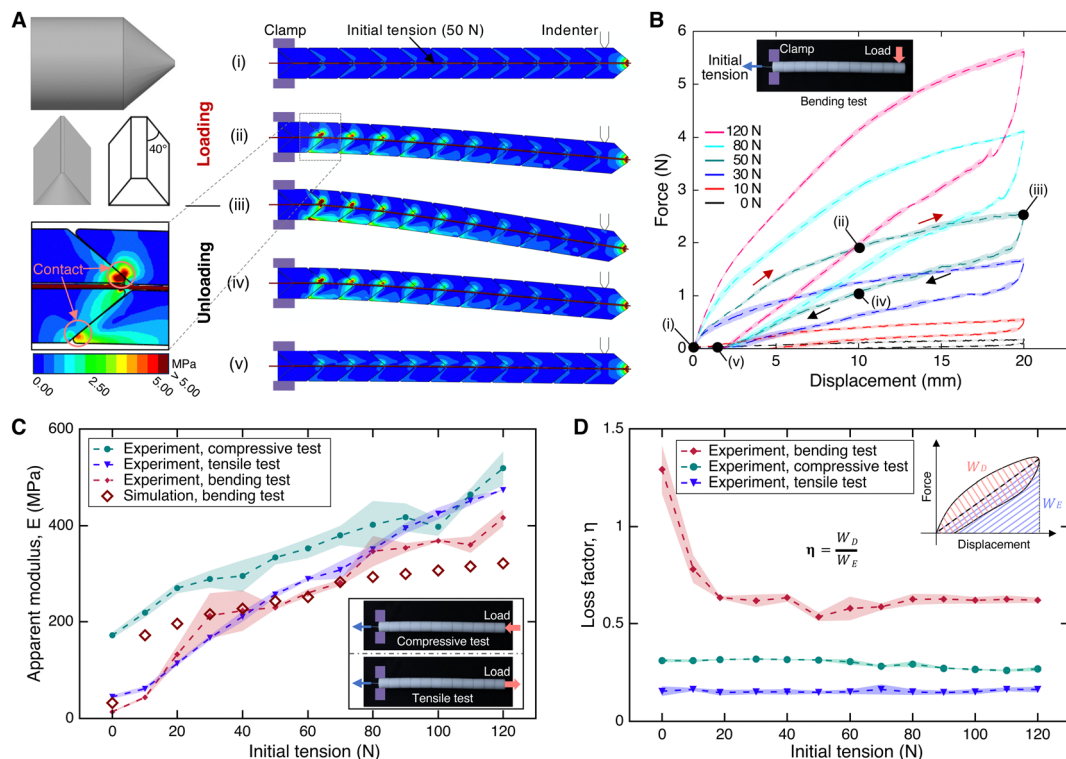
Fig. 2 Characterization of a CCPJ-based beam with variable applied contracting tension. (A) The deformation and von Misses stress distribution of a beam under bending loading and unloading. The beam is composed of 11 concavo–convex beads with a 40° cone angle (CAD model shown in the insert) and the string pretensioned at 50 N. (B) Experimentally measured force–displacement curves at different initial contracting tensions. The coloured dash lines represent the average values, and the shaded areas represent the standard deviations between three different tests. (C) Bending, tensile, and compressive test apparent modulus as a function of the initial contracting tension. The shaded areas represent the standard deviation between three different tests. (D) Loss factor, representing the damping capability, as a function of the contracting tension, for bending, tensile, and compressive tests. The shaded areas are the standard deviation between three different tests.

is fixed to the top bead of the beam. The other end is attached to a force stand. The force stand can adjust the initial tension (small changes in tension occur during testing) applied to the nylon string (see Methods). The applied tension triggers a jamming transition[52] and geometrical interlocking[59,60] among beads which increases the frictional and geometrical contact, turning the beams into load-bearing structures. The beam used in these tests has eleven beads with 40° cone angles (Fig. 2(A), other parameters detailed in ESI,† Table S1).

To quantify the change in mechanical properties as a function of contracting initial tension, we perform one-point bending tests and calculate the apparent elastic bending modulus and loss factor (or energy dissipation coefficient) of the beams (see Methods). In these experiments, the sample is clamped at one end, and a line-shaped indenter is applied to the other end in the middle of the top bead (ESI,† Movie 2).

Before running experiments, we used a finite element (FE) model to visualize the bending process and characterize its underlying mechanism (see Methods). Upon application of a 50 N initial tension on the string, the beam is straight, with stress evenly distributed among the eleven beads (Fig. 2(B)-(i)). When bent, the stress distribution concentrates more on the beads close to the fixed end, but remains well-distributed thanks to the additional frictional contact introduced by the

interlocking geometry (Fig. 2(A)-(ii), (iii)). In comparison to the jamming of conventional non-concave beads, our proposed beads with cone-shaped interfaces introduce two contact areas. This delay in separation between beads helps maintain beam stiffness even at large indentation (ESI,† Text S1). This extended high-stiffness range is advantageous for practical applications where large deformations are often inevitable, and a sudden drop in stiffness could lead to severe failures. During unloading, the tension on the string provides a recovery force to unbend the beam (Fig. 2(A)-(iii)–(v)). Once fully unloaded, a small residual displacement results from the frictional force between beads (Fig. 2(A)-(v), see ESI,† Movie S3 for a full animation). The extracted force–displacement curve of the FE beam shows close agreement with the experimental data (Fig. S2 and S39, ESI†); the calculated apparent bending modulus and loss factor also have small deviations (ESI,† Table S2), suggesting the validity of the FE model.

We then ran the experiments with various initial tensions on the string. The measured force–displacement curves show initially stiffer regimes at small indentation depths (Fig. 2(B)). This linear regime is governed by the elastic behaviour of the jammed granular structure.[52] As indentation increases, we observe a nonlinear response with a consistently decreasing instantaneous stiffness. This phenomenon is likely due to

frictional sliding and local repositioning of the beads.[52] Changes in string tension during indentation are small, so their contribution to this nonlinearity can be considered negligible (Fig. S3, ESI†). As concluded, granular materials are intrinsically discrete and strongly anisotropic,[49,51,60–62] and so are our beams. Here, we use the apparent elastic bending modulus E_b[52,63] and the loss factor η_b[64] as parameters to compare the beams' mechanical properties (see Methods). Specifically, E_b and η_b represent the stiffness and the energy dispassion capabilities, respectively. These two parameters can be calculated as:

$$E_b = \frac{16K_b L^3}{3\pi D_O^4} \qquad (1)$$

$$\eta_b = \frac{W_D}{W_E}, 0 \le \eta_b \le 2 \qquad (2)$$

where K_b is the stiffness of the initial linear regime from the one-point bending test (Fig. 2(B)). L and D_O are the as-fabricated length and outer diameter of the beams (see Methods for more details). W_D is the dissipated/damped energy during the bending process, which is estimated as the area enclosed by the loading curve and the unloading curve. W_E represents the stored energy (see Methods).

As the initial tension increases from 0 N to 120 N, the apparent bending modulus increases monotonically, from about 12.4 MPa to 434.6 MPa, by over 35 times (Fig. 2(C)). Simulations using the FE model were also run (Fig. S38, ESI†) and the approximated apparent bending moduli agree relatively well with experimental results. The increase in bending modulus at high tensions is representative of granular materials and is expected since the grains interact by frictional contact.[49] Under deployed conditions with a small amount of slack present, the stiffness can potentially decrease to an indefinitely low bound; the bending modulus of the sample could be estimated by solely evaluating that of the actuator (i.e., nylon string in this case), which is at the order of 10^{-3} MPa and thus makes the stiffness ratio at the order of 10^5. Here we only quantify the stiffness starting from 0 N tension without slack. The loss factor shows a monotonic drop (from 1.29 to 0.62) at the low tension region and quickly reaches a saturation value as the tension continuously increases, approximately a 52% reduction (Fig. 2(D)). This is because the increasing compressive stress between beads enhances their frictional contact and shifts the major deflection mode from high-damping sliding to low-damping elastic behavior. This shift also explains the decreasing residual deformation as the tension increases. In addition to the wide range of damping variance, the jammed beam shows an overall large loss factor of above 0.6, representing a high damping material.[61,65]

To better understand the performance of the beam, we also perform tensile and compressive tests (ESI,† Movies S4 and S5) and calculate the apparent tensile/compressive modulus and loss factors (see Methods). The measured force–displacement curves (Fig. S4 and S5, ESI†) both show initially linear regimes at small indentation depths and nonlinear responses at large deformation, which is similar to the behavior observed in the bending tests. We obtained increases of about 10 times and 3 times for apparent tensile and compressive modulus, respectively, as the initial tension increases from 0 N to 120 N (Fig. 2(C)). Here, these increases mostly originate from the intrinsic nonlinearity of the constituting materials (nylon and resin) and geometry. The nylon string material has much larger nonlinearity than the resin bead material, giving a higher stiffness tunability for samples under tensile loading (Fig. S6 and S7, ESI†). In addition, the damping in both tensile and compressive tests are low and show very limited tunability (Fig. 2(D)). This is because bending can introduce more nonlinear interfacial interactions between beads (Fig. S31, ESI†), which leads to a larger damping and thus tunability. The influencing factors include interface geometry (i.e., cone angle and edge radius), material properties (i.e., elastic modulus of the beads and string), and contact characteristics (i.e., coefficient of friction between beads and between bead and string). Therefore, by not relying on the nonlinearity of constituting materials, our proposed structured beams have much larger tunability of mechanical properties in bending-dominated configurations rather than stretching-dominated ones. This indicates that we should utilize the bending-dominated mode of the beams to improve the tunability of mechanical properties in the construction of large scale metamaterials.

Effect of the design parameters

The performance of our contracting-cord mechanical metamaterials depends on many factors, including geometry, dimensions, and material properties.[49] We identify the beads' cone angle as the key parameter affecting both self-deployment and mechanical properties tunability (the ability to widely tune the mechanical properties).[60] The effects of other factors, including the beads' Young's modulus, edge radius, beads' length, and friction coefficients, are discussed in ESI,† Text S2 and Text S10.

To explore the relationship between the cone angle and the jammed structure's mechanical properties, we experimentally studied the mechanical responses of beams (with the beads from 30° to 90° with an interval of 10°) under one-point bending at different contracting initial tensions (Fig. S8, ESI†). We also studied the mechanical responses of these beams under tensile and compressive tests, however, these tests did not exhibit as significant of a tunability phenomenon as in the bending tests (Fig. S4 and S5, ESI†), which confirms the conclusion in the last section.

For bending tests, we observed that the tunability of the apparent bending modulus and the tunability of the loss factor show similar trends as cone angles are varied (Fig. 3(A) and (B)). When the angle is small (less than 70°), the neighboring beads permit more complex interactions (i.e., face–face and face–edge contacts) due to their interlocking geometry (Fig. 3(C)). As each bead-to-bead interface contains two distinct contact regions, the beam's tension-controlled stiffness is largely dependent on nonlinear contact effects. The level of nonlinearity increases as the angle decreases, which coincides with the observed phenomenon that the stiffness tunability grows as the angle decreases (in light green in Fig. 3(A)). This same phenomenon
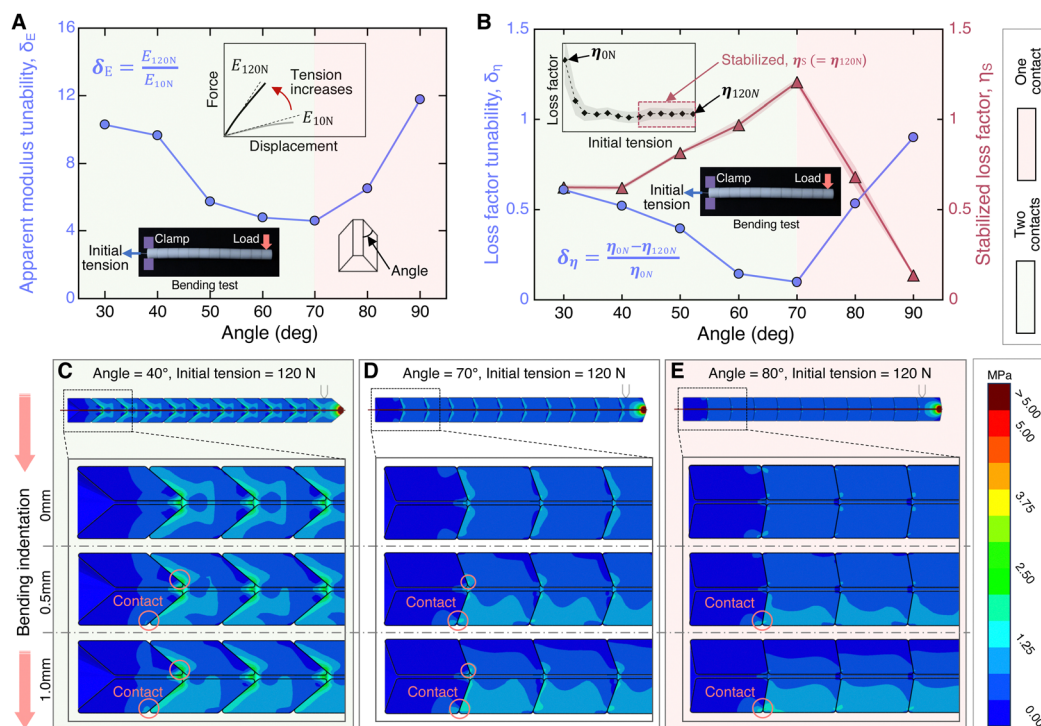
Fig. 3 Relating the tunability of mechanical properties to cone angle. (A) The tunability of the apparent bending modulus, δ_E, as a function of bead cone angle, α, as determined by experimental characterization. δ_E is defined as the ratio of the apparent bending modulus at 120 N over the modulus at 10 N. (B) The tunability of loss factor, δ_η, as a function of bead cone angle for bending tests. The shaded areas represent the standard deviation between three different tests. See Methods for a detailed definition of δ_E and δ_η. (C)–(E) The simulated deformation and von Misses stress distribution of three beams (with beads having 40°, 70°, and 80° cone angles) under bending indentation up to 1 mm. The strings are pretensioned to 120 N.

is often observed in interlocking granular media.[62] There are, however, limitations on the minimum angle value imposed by (i) the feasibility of manufacturing of the beads, and (ii) the excessive contact stresses at the interfaces, which could extensively damage individual beads.[60] At a 70° angle, the jammed system exhibits a transitional behaviour, where the conditions at the conical interfaces shift from two contact areas to one contact area (Fig. 3(D)). When the cone angle is larger than 70°, the behaviour of the beam resembles conventional non-concave particle jamming (with one contact), showing no interlocking (Fig. 3(E)) and presenting unstable slips at large bending indentation (Fig. S8, ESI†). For the area of interest (30–70°), the tunability of damping decreases monotonously as the cone angle increases (in light green in Fig. 3(B)). With large cone angles, the beam benefits less from the additional contact and tends to slip under bending indentation, causing large energy dispassion across different tension levels, which is indicated by the high stabilized loss factors. Thus, these beams with large angles have smaller damping tunability.

Bead cone angle also influences the ease of beam assembly and the alignment accuracy between beads. Here, we vary the bead cone angle (all beads within a single beam have the same cone angle) for self-deployment tests. A one-kilogram weight is tied to the string and released to activate assembly of the beam against gravity (Fig. 4(A) and ESI,† Movie S6, see Methods for detailed operation). Fig. 4(B) and (C) show successfully assembled beams with 40° and 80° cone angles, respectively.

We observed that, at small angles, the last two beads tend to lock easily, which locking cannot be overcome by increasing the tension on the string (Fig. 4(D)). This is probably due to the applied string tension having an extremely short moment arm against the end bead, thus failing to overcome the opposing moments from friction and gravity. We use assembly success rate to quantify the ease of self-deployment. Alignment accuracy is quantified by the alignment error. A small alignment error indicates that the system has high alignment accuracy. The alignment error is defined as the ratio of the misalignment offset to the bead's outer diameter ($\Delta x/D_O$) (Fig. 4(C)). We found that the assembly success rate monotonously increases as the angle increases from 30° to 90° with an interval of 10°. Contrarily, sharper cone angles facilitate bead alignment, which can result in more accurately aligned, and thus more functional, structures (Fig. 4(E)). These two opposite trends caused by cone angle indicate a necessary trade-off between alignment accuracy and success rate for certain self-deployment tasks.

In summary, we explore the complex relationship between beam design parameters and mechanical characteristics. Our results indicate that the bead cone angle controls a trade-off between mechanical properties tunability and self-deployability, which must be considered based on the specific design application.

Characterizing cubic unit cells

Our CCPJ-based beams are fundamental building blocks, which can be assembled into lattices for various applications. Here we
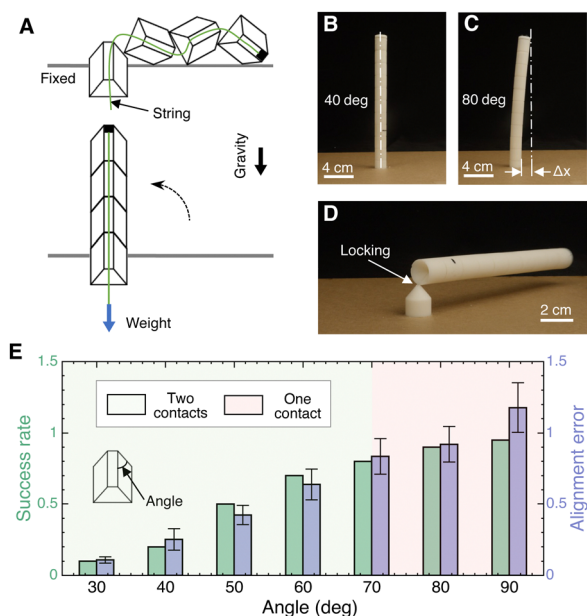
Fig. 4 Characterizing self-deployment of an individual beam. (A) Testing schematic. Beads assemble into a vertical beam against gravity, driven by a nylon string under tension induced by dropping a one-kilogram weight. (B) Image of a deployed beam with beads of 40° cone angle, showing a high alignment accuracy. (C) Image of an assembled beam with beads of 80° cone angle, displaying a large offset, Δx, between the cap and end beads. (D) A typical deployment failure mode—locking occurs mostly between last two beads. (E) Success rate and alignment accuracy as a function of cone angle. The success rate is calculated as the ratio of successful attempts over 20 trials. The alignment error is defined as the ratio of the outer diameter of the beads over the offset ($\Delta x/D_O$). Error bars represent the deviation between three different tests.

demonstrate this capability using 40° beads to create two classes of lattices: bending-dominated cubes and stretching-dominated cubes. A bending-dominated lattice consists of eight CCPJ beams, arranged into two squares on opposite sides of a cube (Fig. 5(A)). Four rigid bars are used to connect these two squares between corresponding nodes. The stretching-dominated lattice differs from the bending-dominated, in that it has two additional diagonal CCPJ beams (Fig. 5(C)). To quantify the characteristics of these lattices, we conducted compressive tests (ESI,† Movie S7) and extracted the force–displacement curves as we varied the contracting tension of each beam (see Methods). For the bending-dominated lattice, the measured force–displacement curves (displacement controlled, in Fig. 5(B)) have initially linear regimes at small indentation while nonlinear responses are observed as displacement increases. As tension increases, the stiffness of the bending-dominated lattice shows a large change while that of the stretching-dominated only has a small increase (Fig. 5(D)). Specifically, the bending-dominated lattice shows an approximately 32 times increase in stiffness as the initial tension changes from 0 N to 120 N. This variance reflects the large stiffness tunability of a single beam (Fig. 5(E)). In contrast, the stretching-dominated lattice exhibits much higher stiffness values[66] but limited tunability (about 5 times increase) as most

beams are in compression. We note that the stiffness of stretching-dominated lattice quickly plateaued at low contracting tensions.

The bending-dominated lattice shows higher damping capability and tunability than the stretching-dominated one, which is consistent with our conclusion from the preceding section: a single beam has larger damping ability and tunability in bending than it does under tensile/compressive loading (Fig. 5(F)). Specifically, the bending-dominated lattice can achieve a ~40% reduction in its loss factor while the loss factor of the stretching-dominated lattice varies inconsistently and within a smaller range. The tendency of damping of the stretching-dominated lattice is also different from the constructing unit beams since beams are mainly subject to compressive or tensile load, instead of bending load.

Actuating functional metamaterials

To autonomously deploy the proposed metamaterials, the actuators need to satisfy several requirements. (i) The contracting parts of the actuators should be string-like to fit into the holes of the beads. (ii) The actuators should be soft and elastic, enabling compact storage, impact resilience, and reversible operation. (iii) The actuators need to be capable of exerting sufficient contracting strain and stress. Here, we choose to use MDCs and SCPAs as example actuators to demonstrate the feasibility of implementing our metamaterial. Each MDC module consists mainly of a motor, a nylon string, and a customized spool (see Methods). When activated, the motor can either pull the string to contract and deploy the beam or release the string to collapse the assembled beam (Fig. 6(A) and ESI,† Movie S8). MDCs exhibit excellent power density at the centimeter scale, fast response speed, and an easy integration interface, making them highly suitable for applications at this scale. SCPAs are conductive and can be electrically/thermally driven, which gives rise to a wide range of applications. To avoid overheating, we used flat plywood beads with this actuator. Once electrical current is applied, the soft assembly of beads becomes rigid (Fig. 6(B)). Upon cutoff of the applied electricity, the beam softens and drops under gravity (ESI,† Movie S9). Smart material-based actuation holds promise for challenging applications, such as small-scale deployments and remote operations in extreme environments, such as areas with strong magnetic fields. Additionally, we assembled twelve such beams into a cube. The cube demonstrated successful self-deployment and subsequent self-collapse controlled by electrical signal, expanding its occupied volume by about 15 times (Fig. 6(C) and ESI,† Movie S10). This feature is especially important for remote deployment applications, where materials may need to be transported in a compact volume and assembled autonomously *in situ* to form functional machines for given tasks.[6]

Next, we demonstrated the viability of creating larger-area (and volume) metamaterials by prototyping a cubic lattice composed of an 2 × 2 × 2 arrangement of unit cells (Fig. 6(D)). We chose to fabricate the lattice with resin beads having 40 degree cone angles for better alignment. For ease of
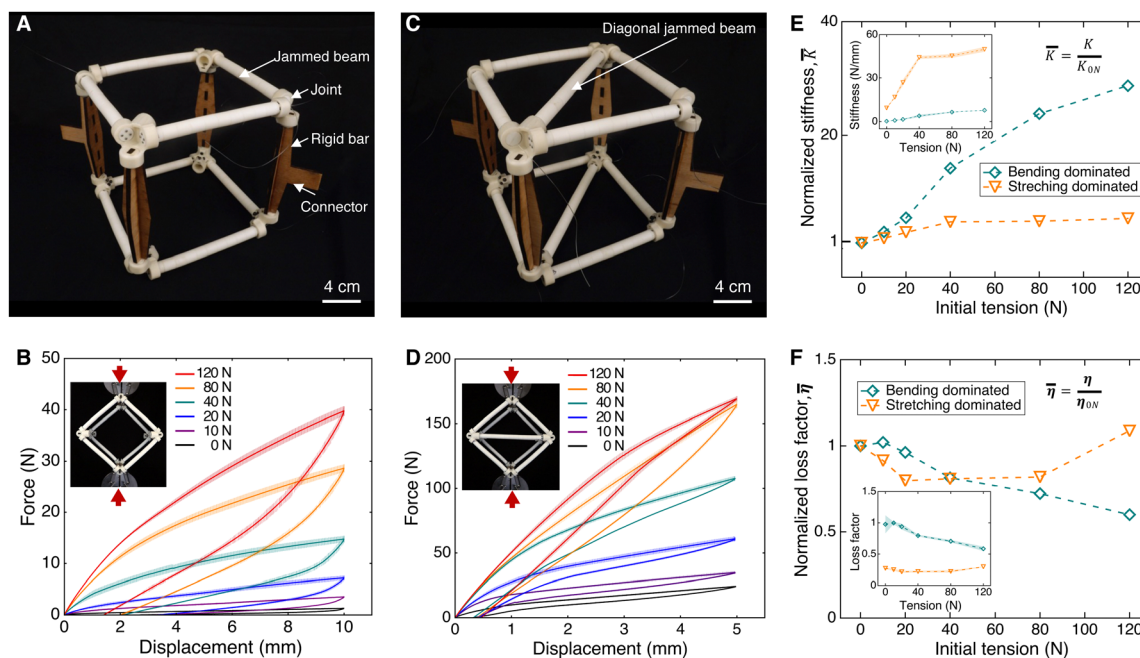
Fig. 5 Characterization of a single metamaterial unit cell. (A) Labeled image of a bending-dominated lattice. Each beam in the lattice was assembled with a pre-tensioned nylon string. Beams were connected into two squares using customized 3D printed joints. Four rigid bars were used to connect these two squares. Two of the rigid bars provide connectors for interfacing with Instron clamps. (B) Measured force−displacement curves at different contracting tensions for the bending-dominated lattice. The coloured lines represent the average values, and the shaded areas represent the standard deviation between three different tests. (C) Image of a stretching-dominated lattice. Two diagonal beams distinguish its structure from the bending-dominated lattice. (D) Measured force−displacement curves at different contracting tensions for the stretching-dominated lattice. The coloured lines represent the average values, and the shaded areas represent the standard deviation between three different tests. (E) Normalized stiffness, $\bar{K}$, of lattices as a function of contracting tension. The stiffness at different contracting tensions is normalized over the stiffness at 0 N tension. The insert shows non-normalized stiffness. (F) Normalized loss factor, $\bar{\eta}$, as a function of contracting tension. The loss factor is normalized over the value at 0 N tension. The insert shows the non-normalized loss factor.

assembly, beads were 3D printed hollow to reduce gravitational forces and their edges were smoothed to avoid locking. For simplicity, we routed several nylon strings through all beads in a specific pattern (see Methods). The soft assembly could be quickly deployed into a large and rigid 2 × 2 × 2 lattice. The lattice increased its volume by ∼14 times and could sustain a dumbbell of 5 pounds (about 13 times its own weight). Upon releasing the tension, the lattice collapsed quickly into its soft state under gravity without requiring external interference (ESI,† Movie S11).

Finally, we demonstrate the tunability of the same 2 × 2 × 2 lattice by comparing its response to an impact load when deployed and under different string tensions (Fig. 1(E), see ESI,† Movie S12 for full process). For each case, we manually drop a ball from a certain height onto the top of the structure. When we deploy the lattice and apply a low string tension, the assembly is compliant, allowing the ball to sink into the lattice. The lattice slows the ball to a stop, capturing it and significantly absorbing its kinetic energy. When the tension is increased, the lattice maintains its shape, but increases in stiffness. When dropped, the ball contacts the lattice and bounces back up. After the task, the lattice can self-retract to its disassembled soft, compact state for easy storage and transportation. Notably, we can dynamically and repeatedly shift between the structure's different states (the undeployed state, the deployed compliant state, and the deployed rigid state) by modifying the contracting tension on the actuators.

Conclusions

We have shown that self-deployable mechanical metamaterials based on contracting-cord particle jamming (CCPJ) can provide on-the-fly continuous tunability of mechanical properties after assembly. These metamaterials are robust to temporary overloading[60] and resilient to damage,[56] attributes that stem largely from their unique configuration. Composed of discrete rigid beads threaded by elastic strings, the system's compliance allows it to withstand instant overload or collision by dissipating energy through frictional sliding rather than fracturing. Moreover, its discretized structure enables it to sustain the loss of several beads without losing functionality. The proposed metamaterials are easily manufacturable and low cost as well. In addition, we have systematically explored the underlying mechanics of CCPJ-based beams during both the self-deployment and the jamming transition processes. Notably, these beams features larger tunability in their bending-dominated configuration than in their stretching-dominated mode. The identified key design parameter, bead cone angle, is also investigated, showing a complex effect on mechanical
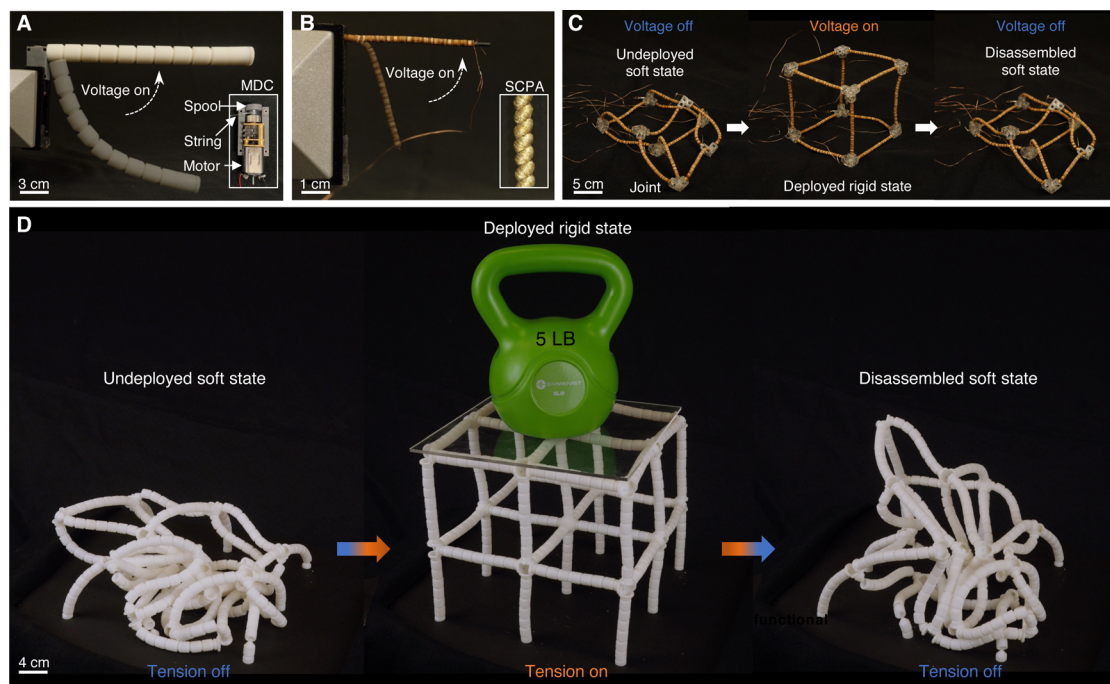
Fig. 6 Actuation and self-assembly of metamaterials and functional devices. (A) Self-deployment of a resin-printed beam actuated by an MDC. The insert shows the composition of an MDC—a DC motor, a spool, and a nylon string. (B) Self-deployment of a plywood beam driven by an SCPA. The insert shows the SCPA, which can be activated electrically or thermally. (C) A cubic lattice can self-deploy and self-collapse by actuating the SCPAs on-demand. The lattice consists of twelve beams (shown in (B)) with eight joints. (D) On-the-fly manipulation of a 2 × 2 × 2 cubic metamaterial. The metamaterial is controlled by nylon strings. Once the strings are tensioned, it quickly transforms from its compact, ultrasoft state to its large-volume, load-bearing state, which can sustain a dumbbell of 5 pounds. Upon release, the metamaterial collapses and returns to its original soft state, ready for subsequent operation.

property tunability and self-deployability. This systematic analysis presents the design space and rules for such CCPJ-based metamaterials.

Deployable lattices with preprogrammed geometry are constructed from concavo–convex beads, demonstrating the viability of creating complex, large-scale CCPJ-based active metamaterials. Recent advances in smart actuators[67–72] and additive manufacturing make it possible, in principle, to automate the fabrication processes and allow large-scale implementation across various dimensions, targeting different applications. Large-scale active metamaterials hold particular promise for space applications, where the constraints of mass and transportation volume are critical, and reducing the effects of gravity can be advantageous.[3,10] Specifically, our mechanism not only addresses issues of mass and volume more effectively than origami-inspired folding methods but also provides tunable stiffness to accommodate changing environments without requiring additional actuation or associated components. With the integration of power and control, it is possible to envision fully programmable mechanical properties and morphologies *via* local tuning of each actuator within the metamaterial. This integration could potentially lead to untethered robotic devices for advanced functionalities, such as locomotion, manipulation, and beyond.[6] In summary, the proposed design paradigm broadens the horizon for designing fully programmable materials, thus offering an impetus to their exploration for practical applications, such as soft robotics, human–machine interaction, medical devices, and space engineering.

Materials and methods

Experiments

Materials and manufacturing. The concavo–convex beads are 3D printed *via* Stereolithography (SLA) 3D printing using a commercial 3D printer (Form 3+, Formlabs). The material used to print the bead is white resin, with a density of 1.15 g cm^{-3}, a tested Young's modulus of 0.571 GPa (S4). The contracting cord for experimental characterization is made of nylon string (30LB, Amazon) with a diameter of 0.55 mm. Each string is securely fixed on top beads with screws (Fig. S9, ESI†). Unless otherwise mentioned, testing samples are composed of eleven resin beads with a nylon string. Detailed parameters are shown in ESI,† Table S1. To better characterize the behaviors, here we apply tension through a nylon string with a fixed length instead of applying constant tension. This setup more accurately simulates practical scenarios—a string-like actuator with a certain length is employed to generate contracting tension. Note that the tension in the string actuator might vary based on the external loading condition. The 90° beads are cut using a laser cutter (Speedy 300TM Flexx, Trotec Laser Inc.) from a 3 mm thick sheet of plywood.

The SCPAs were made using commercially available conductive yarn (235-34 4ply HCB, V Technical Textiles Inc.) with a diameter of about 0.4 mm. These actuators are prepared in two steps (Fig. S10, ESI†).[73] (i) We insert coils by continuously twisting the conductive yarn under a 280-gram weight. The weight is free to move vertically, but not allowed to rotate. (ii) We anneal the coiled yarn with a cyclic heating/cooling process (0.45 A annealing current, 30 s heating, and 30 s cooling per cycle, 8 hours). The prepared actuators have an average diameter of about 0.71 mm. A single SCPA can generate up to 15% tensile strain (with pretension) and a maximum force of around 3 N.

The MDC design is adapted from actuators commonly used for tensegrity robots.[25] They are primarily composed of a DC motor (1000:1 HP 6V, Pololu), a customized spool, and a nylon sting (Fig. 6 and Fig. S11, ESI†). All three components are housed in a 3D printed case. When the motor runs, the spool on the shaft rotates to shorten the nylon string. Due to the small spool diameter, the MDC can output a maximum tension of about 140 N while the string breaks at about 130 N. This output tension is sufficient for most applications.

For cubic unit cells (both bending- and stretching-dominated), the end beads were redesigned into two halves (Fig. S12, ESI†). After the strings were stretched to the desired tension, the other end was clamped by the two halves of the end bead. Screws are used to retain the tension. Then, eight beams with the same applied tension were assembled together with four rigid bars through 3D printed joints (Fig. S13, ESI†).

For the $2 \times 2 \times 2$ cubic lattice, all beads are hollow to reduce the effects of gravity. The bottom edges of the beads are smoothed to improve the ease of self-deployment (Fig. S14 and S15, ESI†). To make the structure symmetric and assembly easier, we introduced center beads with both bases concave. We also designed hollow joints that allow nylon strings to pass through with low friction. Thirteen nylon strings in total are routed to go through every single bead in a special pattern (Fig. S16, ESI†).

Quasi-static mechanical tests. The bending characteristics of the beams at different contracting tensions are characterized *via* one-point bending tests (Fig. S17, ESI†). Test rig design is described in detail in ESI,† Text S3. First, the end bead of each beam is clamped in a vise. One end of a 380 mm-long nylon string is first fixed on the top bead and the other is then fixed on the load cell of a customized force stand through a rigid connector. The load cell is allowed to move to apply a certain tension to the string and then is fastened to the force stand. Thus, the load cell applies displacement constraint to the string instead of force constraint. Different tensions are applied by adjusting the position of force stand's load cell and then fixing it for testing. Note that we straighten the beams before applying an initial tension as gravity can cause a slight bend in the beams before testing. The tests are performed using a universal testing machine (5966, Instron Inc.), with displacement controlled at a loading rate of 10 mm min^{-1}. Three separate tests are repeated at each contracting tension. Before each test, the beams are manually reset to a straight initial configuration.

The coloured lines and dashed areas represent the average values and standard deviations for three different tests (Fig. 2). The deviation observed between the results from different tests at the same tension arises from the initial configurations of the beams, which have different random initial contacts between beads.

Tensile and compressive tests utilize setups akin to those for bending tests, with the primary difference being the fixtures used (Fig. S18, ESI†). Specifically, we rearrange the orientation of the beams and force stand due to the limited space within the testing machine. We place a low-friction pulley within the end bead clamp to reorient the direction of the nylon string's tension. For tensile tests, we designed a connector to grab the top beads and a base to clamp the end beads. For compressive tests, we redesigned the base to allow for direct contact between end beads and the steel clamp of the testing machine, thus eliminating undesired testing errors from fixtures.

The compressive tests for cubic lattices were conducted in the same machine with their connectors (on rigid bars) clamped onto the grippers of the Instron machine. The tests were run with displacement controlled at a loading rate of 10 mm min^{-1}. Similarly, each tension was repeated three times with the lattices reset to the original configuration between tests.

Calculating the apparent modulus of CCPJ beams. The stiffness of the initial elastic region in our bending measurement was calculated by fitting the force–displacement curve linearly (Fig. 2) for small indentation depths (between contact and 0.5 mm). These shallow indentations result in in-plane strains of less than 0.05%, guaranteeing that the beams experience deformation within their elastic threshold. The apparent bending modulus is computed according to eqn (1), using the measured dimensions and stiffness (slope) of the elastic regime. For apparent tensile and compressive modulus, we apply similar methods according to below equation:

$$E_t = \frac{4K_t L}{\pi D_O^2} \tag{3}$$

$$E_c = \frac{4K_c L}{\pi D_O^2} \tag{4}$$

where K_t and K_c are the respective stiffnesses of the linear regime from the tensile and compressive one-point bending tests (Fig. 2(C) and (D)).

Calculating the stiffness of cubic lattices. We linearly fit the selected regime (ranging from 0 to 1.0 mm) of the force–displacement curves obtained from the compressive measurements (Fig. 5). The slopes are the stiffness of interest, normalized by the stiffness when the internal tensions of beads are 0 N.

Calculating the loss factor. We programmed a code in Python to integrate the total enclosed areas that represent dissipated energy W_D and the stored energy W_E (Fig. S19, ESI†). Specifically, the stored energy is approximated as the sum of half of W_D and the area under the unloading curve according to ref. 64. The loss factors for all three different tests (*i.e.*, bending, tensile, and compressive) were calculated using eqn (2). Although there are different ways to define the loss factor, they

all yield similar results. Consequently, we choose to only focus on the method stated above.

Calculating the tunability of apparent modulus and loss factor. Tunability refers to the extent to which mechanical properties can be altered in response to increases in the initial tension applied to the contracting cord. For the tunability of apparent modulus, we used the modulus value of the beam at 10 N as the reference. This is because the apparent moduli at low tensions (close to 0 N) are rather unstable. The maximum initial tension on the string is 120 N. Thus the apparent modulus tunability, δ_E is defined as:

$$\delta_E = \frac{E_{120N}}{E_{10N}} \tag{5}$$

Here, we used the values of loss factors at 0 N as the reference since loss factors are relatively stable even at low tensions. Therefore, the loss factor tunability, δ_η, is:

$$\delta_\eta = \frac{\eta_{0N} - \eta_{120N}}{\eta_{0N}} \tag{6}$$

Self-assembly test and characterization. We used the same beams (with eleven beads) to characterize the performance of self-assembly. The beams were oriented vertically with the end beads fixed to a rigid platform. A one-kilogram weight was fixed to the end of the nylon string. When tested, the weight was released to generate tension to drive the assembly. We repeated this process 20 times for each angle and calculated the success rate.

The alignment error is defined according to the equation below:

$$A_{error} = \frac{\Delta x}{D_O} \tag{7}$$

Δx is the offset between the top bead and end bead (Fig. 4(C)), which is extracted from video using the tracking software Tracker (version 5.0.5). D_O is the outer diameter of the beads. The measurement for offset was repeated three times for each angle. Before each test, the beads were randomly shuffled.

Numerical simulations

Finite element CCPJ beam construction. Finite element (FE) models were created using the commercially available ABAQUS CAE software.[74] The models match the geometry of the CCPJ beams that were experimentally tested on the universal testing machine, where beams are constructed of eleven beads having a cone angle in the range of $30°$ to $90°$ (Fig. S20, ESI†).

Beads are meshed using 8-node 3D deformable linear brick elements with reduced integration (C3D8R). Each is assigned a linear elastic, isotropic material model with a mass density of 1.15 g cm^{-3} and 0.57 GPa Young's modulus to match the experimentally determined values (ESI,† Text S4). A Poisson ratio of 0.4 is also assigned.[75] The string is modeled using a fine mesh of 2-node linear 3D truss elements (T3D2). Its material is modeled as hyperelastic using an Ogden model fitted to experimental data (ESI,† Text S5). The indenter is modeled as a 3D analytical rigid body (Fig. S20, ESI†).

Strain free adjustments are allowed between beads in the first load step to initiate contact. All contact interactions are assigned a hard normal behavior and a tangential friction coefficient. Bead-bead interactions are assigned a coefficient of 0.15 as determined by parametric FE studies (ESI,† Text S2). Bead-string and indenter-bead contact interactions are assigned a coefficient of 0.1, which is decided based on the same parametric FE studies (ESI,† Text S2).

Quasi-static bending simulation. Loading conditions in the FE analyses are equivalent to those of the quasi-static bending tests performed on the universal testing machine. The results enable analysis of the underlying mechanics of the experimental response. Each simulation is composed of three load steps: tensioning, indentation, and return. Each step is a quasi-static dynamic implicit procedure with geometric nonlinearity.

During the first step, a tensioning displacement is gradually applied to one end of the string of 380 mm, while the outer surface of the rear bead is fixed in all degrees of freedom (Fig. S21, ESI†). The displacement load corresponds to an applied string tension between 1 N and 120 N as determined in a separately conducted analysis (Fig. S22, ESI†). The other end of the string is rigidly secured to the tip of the front bead *via* multi-point constraints. During the deflection step, the indenter is displaced in the negative vertical direction at 10 mm min^{-1} for 20 mm. During the return step, the indenter returns to zero displacement at the same rate (ESI,† Movie S3 and S13).

Parametric studies. Using custom MATLAB and Python scripts to interface with the ABAQUS FE model, we studied trends in quasi-static bending behavior when varying the following parameters: bead cone angle, string tension, bead Young's modulus, bead-bead friction coefficient, and bead edge radius (see ESI,† Text S2 for detailed exploration).

Author contributions

Conceptualization: J. B. H.; planning: W. Y., J. B. H., and A. M.; experimentation: W. Y., C. J., and R. H. L.; data analysis: W. Y.; simulation: T. J.; demonstration: W. Y.; writing: W. Y. and T. J.; Project management: W. Y., J. B. H., and A. M.

Data availability

The main data and models supporting the findings of this study are available within the paper and ESI.† Further information is available from the corresponding author upon reasonable request.

Conflicts of interest

The authors declare no competing interests.

Acknowledgements

References

1 J. F. Vincent, *Deployable Structures*, Springer, Vienna, 2001, pp. 37–50.

2 J. A. Faber, A. F. Arrieta and A. R. Studart, Bioinspired spring origami, *Science*, 2018, **359**, 1386–1391.

3 S. Pellegrino, *Deployable structures*, Springer, Vienna, 2001, pp. 1–35.

4 G. M. Whitesides and B. Grzybowski, Self-assembly at all scales, *Science*, 2002, **295**, 2418–2421.

5 S. Xu, Z. Yan, K.-I. Jang, W. Huang, H. Fu, J. Kim, Z. Wei, M. Flavin, J. McCracken and R. Wang, *et al.*, Assembly of micro/nanomaterials into complex, three-dimensional architectures by compressive buckling, *Science*, 2015, **347**, 154–159.

6 S. Felton, M. Tolley, E. Demaine, D. Rus and R. Wood, A method for building self-folding machines, *Science*, 2014, **345**, 644–646.

7 Q. Liu, W. Wang, M. F. Reynolds, M. C. Cao, M. Z. Miskin, T. A. Arias, D. A. Muller, P. L. McEuen and I. Cohen, Micrometer-sized electrically programmable shape-memory actuators for low-power microrobotics, *Sci. Robot.*, 2021, **6**, eabe6663.

8 T. Chen, O. R. Bilal, R. Lang, C. Daraio and K. Shea, Autonomous deployment of a solar panel using elastic origami and distributed shape-memory-polymer actuators, *Phys. Rev. Appl.*, 2019, **11**, 064069.

9 S.-J. Kim, D.-Y. Lee, G.-P. Jung and K.-J. Cho, An origami-inspired, self-locking robotic arm that can be folded flat, *Sci. Robot.*, 2018, **3**, eaar2915.

10 H. Mallikarachchi and S. Pellegrino, Design of ultrathin composite self-deployable booms, *J. Spacecr. Rockets*, 2014, **51**, 1811–1821.

11 R. Lakes, Foam structures with a negative Poisson's ratio, *Science*, 1987, **235**, 1038–1040.

12 X. Zheng, H. Lee, T. H. Weisgraber, M. Shusteff, J. DeOtte, E. B. Duoss, J. D. Kuntz, M. M. Biener, Q. Ge and J. A. Jackson, *et al.*, Ultralight, ultrastiff mechanical metamaterials, *Science*, 2014, **344**, 1373–1377.

13 T. Bückmann, M. Kadic, R. Schittny and M. Wegener, Mechanical cloak design by direct lattice transformation, *Proc. Natl. Acad. Sci. U. S. A.*, 2015, **112**, 4930–4934.

14 X. Fang, J. Wen, L. Cheng, D. Yu, H. Zhang and P. Gumbsch, Programmable gear-based mechanical metamaterials, *Nat. Mater.*, 2022, 1–8.

15 Z. Zhai, Y. Wang and H. Jiang, Origami-inspired, on-demand deployable and collapsible mechanical metamaterials with tunable stiffness, *Proc. Natl. Acad. Sci. U. S. A.*, 2018, **115**, 2032–2037.

16 M. Kadic, G. W. Milton, M. van Hecke and M. Wegener, 3d metamaterials, *Nat. Rev. Phys.*, 2019, **1**, 198–210.

17 P. Jiao, J. Mueller, J. R. Raney, X. Zheng and A. H. Alavi, Mechanical metamaterials and beyond, *Nat. Commun.*, 2023, **14**, 6004.

18 J. Park, G. Lee, H. Kwon, M. Kim and J. Rho, All-polarized elastic wave attenuation and harvesting via chiral mechanical metamaterials, *Adv. Funct. Mater.*, 2024, 2403550.

19 J. Park, D. Lee, Y. Jang, A. Lee and J. Rho, Chiral trabeated metabeam for low-frequency multimode wave mitigation via dual-bandgap mechanism, *Commun. Phys.*, 2022, **5**, 194.

20 X. Xia, C. M. Spadaccini and J. R. Greer, Responsive materials architected in space and time, *Nat. Rev. Mater.*, 2022, **7**, 683–701.

21 K. Bertoldi, V. Vitelli, J. Christensen and M. Van Hecke, Flexible mechanical metamaterials, *Nat. Rev. Mater.*, 2017, **2**, 1–11.

22 W. Wang, H. Rodrigue and S.-H. Ahn, Deployable soft composite structures, *Sci. Rep.*, 2016, **6**, 20869.

23 Z. You and Y. Chen, *Motion structures: deployable structural assemblies of mechanisms*, Taylor & Francis, London, 2012.

24 Z. Meng, X. Gao, H. Yan, M. Liu, H. Cao, T. Mei and C. Q. Chen, Cage-shaped self-folding mechanical metamaterials, *Int. J. Solids Struct.*, 2023, 112560.

25 D. S. Shah, J. W. Booth, R. L. Baines, K. Wang, M. Vespignani, K. Bekris and R. Kramer-Bottiglio, Tensegrity robotics, *Soft Robot.*, 2022, **9**, 639–656.

26 S. Spiegel, J. Sun and J. Zhao, A shape-changing wheeling and jumping robot using tensegrity wheels and bistable mechanism, *IEEE ASME Trans. Mechatron.*, 2023, 2073–2082.

27 J. Kim, D.-Y. Lee, S.-R. Kim and K.-J. Cho, A self-deployable origami structure with locking mechanism induced by buckling effect, 2015 *IEEE International Conference on Robotics and Automation* (ICRA) (IEEE, 2015), pp. 3166-3171.

28 Z. Meng, M. Liu, H. Yan, G. M. Genin and C. Q. Chen, Deployable mechanical metamaterials with multistep programmable transformation, *Sci. Adv.*, 2022, **8**, eabn5460.

29 H. Fu, K. Nan, W. Bai, W. Huang, K. Bai, L. Lu, C. Zhou, Y. Liu, F. Liu and J. Wang, *et al.*, Morphable 3d mesostructures and microelectronic devices by multistable buckling mechanics, *Nat. Mater.*, 2018, **17**, 268–276.

30 E. Hawkes, B. An, N. M. Benbernou, H. Tanaka, S. Kim, E. D. Demaine, D. Rus and R. J. Wood, Programmable matter by folding, *Proc. Natl. Acad. Sci. U. S. A.*, 2010, **107**, 12441–12445.

31 J. Sun, E. Lerner, B. Tighe, C. Middlemist and J. Zhao, Embedded shape morphing for morphologically adaptive robots, *Nat. Commun.*, 2023, **14**, 6023.

32 K. Liu, J. Wu, G. H. Paulino and H. J. Qi, Programmable deployment of tensegrity structures by stimulus-responsive polymers, *Sci. Rep.*, 2017, **7**, 3511.

33 A. Kotikian, C. McMahan, E. C. Davidson, J. M. Muhammad, R. D. Weeks, C. Daraio and J. A. Lewis, Untethered soft robotic matter with passive control of shape morphing and propulsion, *Sci. Robot.*, 2019, **4**, eaax7044.

34 Y. Kim, H. Yuk, R. Zhao, S. A. Chester and X. Zhao, Printing ferromagnetic domains for untethered fast-transforming soft materials, *Nature*, 2018, **558**, 274–279.

35 D. Melancon, B. Gorissen, C. J. Garca-Mora, C. Hoberman and K. Bertoldi, Multistable inflatable origami structures at the metre scale, *Nature*, 2021, **592**, 545–550.

36 Z. Zhai, Y. Wang, K. Lin, L. Wu and H. Jiang, *In situ* stiffness manipulation using elegant curved origami, *Sci. Adv.*, 2020, **6**, eabe2000.

37 D. Zappetti, S. H. Jeong, J. Shintake and D. Floreano, Phase changing materials-based variable-stiffness tensegrity structures, *Soft Robot.*, 2020, **7**, 362–369.

38 Y.-J. Park, T. M. Huh, D. Park and K.-J. Cho, Design of a variable-stiffness flapping mechanism for maximizing the thrust of a bio-inspired underwater robot, *Bioinspiration Biomimetics*, 2014, **9**, 036002.

39 D. Zappetti, R. Arandes, E. Ajanic and D. Floreano, Variable-stiffness tensegrity spine, *Smart Mater. Struct.*, 2020, **29**, 075013.

40 J. T. Overvelde, J. C. Weaver, C. Hoberman and K. Bertoldi, Rational design of reconfigurable prismatic architected materials, *Nature*, 2017, **541**, 347–352.

41 R. Baines, S. K. Patiballa, J. Booth, L. Ramirez, T. Sipple, A. Garcia, F. Fish and R. Kramer-Bottiglio, Multi-environment robotic transitions through adaptive morphogenesis, *Nature*, 2022, **610**, 283–289.

42 R. MacCurdy, J. Lipton, S. Li and D. Rus, Printable programmable viscoelastic materials for robots, 2016 *IEEE/RSJ International Conference on Intelligent Robots and Systems (IROS)* (IEEE, 2016), pp. 2628-2635.

43 L. A. Costa, B. Rangel Carvalho, J. Lino Alves, A. T. Marques, A. F. B. da Silva, P. Esfandiari, J. F. M. da Silva, A. Rita Silva and M. Parente, 4D structures for the short-time building of emergency shelters, *Proc. Inst. Mech. Eng., Part L*, 2022, **236**, 1869–1894.

44 L. Zhao, Y. Wu, W. Yan, W. Zhan, X. Huang, J. Booth, A. Mehta, K. Bekris, R. Kramer-Bottiglio and D. Balkcom, Starblocks: Soft actuated self-connecting blocks for building deformable lattice structures, *IEEE Robot. Autom. Lett.*, 2023, 4521–4528.

45 W. Yan, K. Shaposhnikov, P. Yu, Y. Ma and J. Hong, Experimental investigation and numerical analysis on influence of foundation excitation on the dynamics of the rotor system, *Turbo Expo: Power for Land, Sea, and Air*, American Society of Mechanical Engineers, 2015, vol. 56765, p.V07AT30A008.

46 J. Hong, W. Yan, Y. Ma, D. Zhang and X. Yang, Experimental investigation on the vibration tuning of a shell with a shape memory alloy ring, *Smart Mater. Struct.*, 2015, **24**, 105007.

47 S. Mintchev, M. Salerno, A. Cherpillod, S. Scaduto and J. Paik, A portable three-degrees-of-freedom force feedback origami robot for human–robot interactions, *Nat. Mach. Intell.*, 2019, **1**, 584–593.

48 T. Wang, H. Ugurlu, Y. Yan, M. Li, M. Li, A.-M. Wild, E. Yildiz, M. Schneider, D. Sheehan and W. Hu, *et al.*, Adaptive wireless millirobotic locomotion into distal vasculature, *Nat. Commun.*, 2022, **13**, 4465.

49 Y. Jiang, D. Chen, C. Liu and J. Li, Chain-like granular jamming: a novel stiffness-programmable mechanism for soft robotics, *Soft Robot.*, 2019, **6**, 118–132.

50 R. Mukaide, M. Watanabe, K. Tadakuma, Y. Ozawa, T. Takahashi, M. Konyo and S. Tadokoro, Radial-layer jamming mechanism for string configuration, *IEEE Robot. Autom. Lett.*, 2020, **5**, 5221–5228.

51 X. Yang, M. Liu, B. Zhang, Z. Wang, T. Chen, Y. Zhou, Y. Chen, K. J. Hsia and Y. Wang, Hierarchical tessellation enables programmable morphing matter, *Matter*, 2024, **7**, 603–619.

52 Y. Wang, L. Li, D. Hofmann, J. E. Andrade and C. Daraio, Structured fabrics with tunable mechanical properties, *Nature*, 2021, **596**, 238–243.

53 J. R. Amend, E. Brown, N. Rodenberg, H. M. Jaeger and H. Lipson, A positive pressure universal gripper based on the jamming of granular material, *IEEE Transactions on Robotics*, 2012, **28**, 341–350.

54 A. Cavallo, M. Brancadoro, S. Tognarelli and A. Menciassi, A soft retraction system for surgery based on ferromagnetic materials and granular jamming, *Soft Robot.*, 2019, **6**, 161–173.

55 V. Beatini and G. Royer-Carfagni, Cable-stiffened foldable elastica for movable structures, *Eng. Struct.*, 2013, **56**, 126–136.

56 A. V. Dyskin, Y. Estrin, A. J. Kanel-Belov and E. Pasternak, Toughening by fragmentation—how topology helps, *Adv. Eng. Mater.*, 2001, **3**, 885–888.

57 W. Yan, S. Li, M. Deguchi, Z. Zheng, D. Rus and A. Mehta, Origami-based integration of robots that sense, decide, and respond, *Nat. Commun.*, 2023, **14**, 1553.

58 A. J. Liu and S. R. Nagel, Jamming is not just cool any more, *Nature*, 1998, **396**, 21–22.

59 M. Monsef Khoshhesab and Y. Li, Mechanical modeling of fractal interlocking, *ASME International Mechanical Engineering Congress and Exposition*, American Society of Mechanical Engineers, 2017, vol. 58448, p.V009T12A001.

60 A. N. Karuriya and F. Barthelat, Granular crystals as strong and fully dense architectured materials, *Proc. Natl. Acad. Sci. U. S. A.*, 2023, **120**, e2215508120.

61 K. Fu, Z. Zhao and L. Jin, Programmable granular metamaterials for reusable energy absorption, *Adv. Funct. Mater.*, 2019, **29**, 1901258.

62 A. G. Athanassiadis, M. Z. Miskin, P. Kaplan, N. Rodenberg, S. H. Lee, J. Merritt, E. Brown, J. Amend, H. Lipson and H. M. Jaeger, Particle shape effects on the stress response of granular packings, *Soft Matter*, 2014, **10**, 48–59.

63 C. F. Strength, Modulus, and properties of fabric-reinforced laminates, *Composite Materials, Testing and Design*, 1979, p.228.

64 Q. Zhang, X. Yu, F. Scarpa, D. Barton, Y. Zhu, Z.-Q. Lang and D. Zhang, A dynamic poroelastic model for auxetic polyurethane foams involving viscoelasticity and pneumatic damping effects in the linear regime, *Mech. Syst. Signal Process.*, 2022, **179**, 109375.

65 Y. Ma, W. Hu, D. Zhang, Q. Zhang and J. Hong, Tunable mechanical characteristics of a novel soft magnetic entangled metallic wire material, *Smart Mater. Struct.*, 2016, **25**, 095015.

66 A. Alghamdi, T. Maconachie, D. Downing, M. Brandt, M. Qian and M. Leary, Effect of additive manufactured lattice defects on mechanical properties: an automated method for the enhancement of lattice geometry, *Int. J. Adv. Manuf. Tech.*, 2020, **108**, 957–971.

67 C. Hong, Z. Ren, C. Wang, M. Li, Y. Wu, D. Tang, W. Hu and M. Sitti, Magnetically actuated gearbox for the wireless control of millimeter-scale robots, *Sci. Robot.*, 2022, **7**, eabo4401.

68 Q. He, Z. Wang, Y. Wang, Z. Wang, C. Li, R. Annapooranan, J. Zeng, R. Chen and S. Cai, Electrospun liquid crystal elastomer microfiber actuator, *Sci. Robot.*, 2021, **6**, eabi9704.

69 L. Dong, M. Ren, Y. Wang, J. Qiao, Y. Wu, J. He, X. Wei, J. Di and Q. Li, Self-sensing coaxial muscle fibers with bilengthwise actuation, *Mater. Horiz.*, 2021, **8**, 2541–2552.

70 M. Xu, L. Li, W. Zhang, Z. Ren, J. Liu, C. Qiu, L. Chang, Y. Hu and Y. Wu, Mxene-based soft actuators with multiresponse and diverse applications by a simple method, *Macromol. Mater. Eng.*, 2023, **308**, 2300200.

71 L. Xu, H. Zheng, F. Xue, Q. Ji, C. Qiu, Q. Yan, R. Ding, X. Zhao, Y. Hu and Q. Peng, *et al.*, Bioinspired multistimulus responsive mxene-based soft actuator with self-sensing function and various biomimetic locomotion, *J. Chem. Eng.*, 2023, **463**, 142392.

72 D. Wu, Y. Zhang, H. Yang, A. Wei, Y. Zhang, A. Mensah, R. Yin, P. Lv, Q. Feng and Q. Wei, Scalable functionalized liquid crystal elastomer fiber soft actuators with multistimulus responses and photoelectric conversion, *Mater. Horiz.*, 2023, **10**, 2587–2598.

73 W. Yan and A. Mehta, A cut-and-fold self-sustained compliant oscillator for autonomous actuation of origami-inspired robots, *Soft Robot.*, 2022, **9**, 871–881.

74 *ABAQUS Analysis User's Manual, Version 6.6, Section 17.5.1*, Dassault Systemes Simulia Corp, United States, 2006.

75 M. Bodaghi, A. Serjouei, A. Zolfagharian, M. Fotouhi, H. Rahman and D. Durand, Reversible energy absorbing meta-sandwiches by fdm 4d printing, *Int. J. Mech. Sci.*, 2020, **173**, 105451.